Conditional Autoencoder for Generating BNS Waveforms with Tidal and Precession Effects

Mengfei Sun,[1, 2] Jie Wu,[1, 2] Jin Li,[1, 2, *] Brendan Mccane,[3] Nan Yang,[4, 2] Xianghe Ma,[1, 2] Borui Wang,[5] and Minghui Zhang[6]

[1] *Department of Physics,Chongqing University, Chongqing 401331, P.R. China*
[2] *Chongqing Key Laboratory for Strongly Coupled Physics,*
Chongqing University, Chongqing 401331, P.R. China
[3] *School of Computing, University of Otago, Otago 9016, New Zealand*
[4] *Department of Electronical Information Science and Technology, Xingtai University, Xingtai 054001, P.R. China*
[5] *Department of Earth and Sciences, Southern University of Science and Technology, Shenzhen 518055, P.R. China*
[6] *Department of Physics, Southern University of Science and Technology, Shenzhen 518055, P.R. China*

(Dated: March 26, 2025)

Gravitational waves from binary neutron star mergers provide insights into dense matter physics and strong-field gravity, but waveform modeling remains computationally challenging. We develop a deep generative model for gravitational waveforms from BNS mergers, covering the late inspiral, merger, and ringdown, incorporating precession and tidal effects. Using the conditional autoencoder, our model efficiently generates waveforms with high fidelity across a broad parameter space, including component masses (m_1, m_2), spin components $(S_{1x}, S_{1y}, S_{1z}, S_{2x}, S_{2y}, S_{2z})$ and tidal deformability (Λ_1, Λ_2). Trained on 3×10^5 waveforms from the IMRPhenomXP_NRTidalv2 waveform model, it achieves an average overlap accuracy of 99.6% on the test set. The model significantly accelerates waveform generation. For a single sample, it requires 0.12 seconds (s), compared to 0.38 s for IMRPhenomXP_NRTidalv2 and 0.62 s for IMRPhenomPv2_NRTidal, making it approximately 3 to 5 times faster. When generating 10^3 waveforms, the network completes the task in 0.86 s, while traditional waveform approximation methods take over 46–53 s. Our model achieves a total time of 7.48 s to generate 10^4 such waveforms, making it about 60 to 65 times faster than traditional waveform approximation methods. This speed advantage enables rapid parameter estimation and real-time gravitational wave searches. With higher precision, it will support low-latency detection and broader applications in multi-messenger astrophysics.

I. INTRODUCTION

Since the first direct detection of the binary black hole (BBH) merger GW150914 by LIGO and Virgo in 2015 [1], gravitational wave (GW) astronomy has entered a new era, enabling direct exploration of extreme astrophysical phenomena. With continuous advancements in detector sensitivity, an increasing number of BBH and binary neutron star (BNS) mergers have been observed [2–4], providing valuable constraints on the equation of state (EoS) of nuclear matter and insights into tidal interactions in neutron stars [2, 5]. BNS mergers serve as natural laboratories for testing general relativity in the strong-field regime and probing high-density nuclear matter [6]. In particular, measurements of tidal deformability impose stringent constraints on the nuclear EoS, shedding light on neutron star structure and ultra-dense matter properties [7, 8]. Additionally, multi-messenger observations, which combine gravitational waves with electromagnetic counterparts, offer an independent method for measuring cosmological parameters, including the Hubble constant [9, 10].

Due to the significance of BNS systems, accurately modeling gravitational waveforms from their mergers is essential for both detection sensitivity and parameter estimation precision. GW searches rely on matched filtering techniques, which require highly accurate waveform templates, while extracting key physical parameters—such as masses, spins, and tidal deformabilities—demands waveform models with high fidelity. However, modeling BNS waveforms remains challenging due to complex physical effects, particularly spin precession and tidal interactions [11–13]. Waveform modeling has progressed from computationally expensive numerical relativity (NR) simulations [14–16], which solve Einstein's equations directly, to more efficient semi-analytical methods. NR simulations provide high-precision waveforms by capturing strong-field and nonlinear effects but are too costly for large-scale parameter-space studies. Post-Newtonian (PN) approximations [17, 18] describe the inspiral phase analytically under weak-field and slow-motion assumptions but lose accuracy near merger. The effective-one-body (EOB) approach [19–21] improves upon PN by mapping the two-body problem to an effective single-body motion in a modified spacetime. With NR calibrations, EOB models achieve a balance between accuracy and efficiency. Phenomenological models (IMRPhenom) [12, 22–24] further enhance computational efficiency by fitting frequency-domain waveform templates to extensive datasets. These models enable rapid waveform generation, facilitating large-scale searches. Despite advancements, challenges remain in

[*] cqujinli1983@cqu.edu.cn

computational cost, accuracy, and full parameter-space coverage [25–27], limiting real-time GW detection and precise parameter estimation.

The rapid development of deep learning has introduced an efficient and accurate approach to gravitational waveform modeling [28–31]. With strong nonlinear fitting capabilities and high computational efficiency [32], deep learning enables high-precision waveform generation at significantly reduced computational cost. George et al. [33] first applied deep learning to BBH waveforms, achieving real-time performance beyond traditional methods. Schmidt et al. [34] used principal component analysis (PCA) with machine learning to reduce the dimensionality of EOB waveforms, improving computational efficiency. Dax et al. [35] further accelerated waveform generation by leveraging the JAX framework, enabling highly efficient computation and real-time inference. Beyond BBH systems, deep learning has shown promise in BNS and extreme mass-ratio inspirals (EMRIs) waveform modeling. Whittaker et al. [36] employed a conditional variational autoencoder (cVAE) to model post-merger signals, capturing uncertainties in the EoS for probabilistic waveform generation. Chua et al. [37] combined reduced-order modeling with deep learning to accelerate waveform generation for EMRIs, reducing the computational cost of fully relativistic waveforms for LISA data analysis by more than four orders of magnitude. These studies indicate that deep learning accelerates waveform generation and generalizes well across high-dimensional parameter spaces, providing an efficient framework for waveform generation.

Despite progress in deep learning-based waveform modeling, most existing models focus on BBH systems or simplified BNS mergers, with precession and tidal effects remaining underexplored. To address this, we propose a Conditional Autoencoder (cAE) framework for rapid BNS waveform generation, with applications in GW data analysis. Our model efficiently generates waveforms conditioned on system parameters (Θ), including component masses (m_1, m_2), spin components ($S_{1x}, S_{1y}, S_{1z}, S_{2x}, S_{2y}, S_{2z}$), and tidal deformability (Λ_1, Λ_2), while capturing the high-dimensional evolution of GW signals. Trained on a dataset of 3×10^5 BNS waveforms from the IMRPhenomXP_NRTidalv2 [38] model, it includes both precession and tidal effects. To enhance learning efficiency, we adopt the amplitude (A)-phase (Φ) representation, where the polarization waveforms $h_+(t)$ and $h_\times(t)$ are expressed in terms of amplitude and phase independently, to reduce data oscillation. The cAE architecture employs a dual-encoder structure, separately encoding physical parameters and waveform data, which are mapped in latent space before reconstruction. By relying solely on forward propagation, cAE achieves exceptional acceleration in large-scale waveform generation. Benchmark tests on an NVIDIA RTX 3090 GPU and an Intel Xeon Silver 4214R CPU show that for generating a single waveform, cAE requires only 0.12 s, while IMRPhenomPv2_NRTidal and IMRPhenomXP_NRTidalv2 take 0.62 s and 0.38 s, respectively, making cAE approximately 5 times faster. For generating 10^4 waveforms in batch, cAE completes the task in 7.48 s, compared to 497.75 s for IMRPhenomPv2_NRTidal and 454.51 s for IMRPhenomXP_NRTidalv2, yielding speed-ups of about 65 and 60 times, respectively. The model's accuracy is evaluated through waveform overlap calculations, yielding an average mismatch of 3.97×10^{-3}, corresponding to accuracy 99.6%. These results demonstrate that the proposed framework enables efficient, accurate, and scalable BNS waveform generation with precession and tidal effects, making it well-suited for real-time signal detection and parameter estimation.

The structure of the article is as follows: Section 2 describes the waveform representation and the construction of our dataset. Section 3 introduces the fundamental concepts of autoencoders and presents the architecture and hyperparameter settings of our neural network. Section 4 details the model training and validation process. Section 5 evaluates the accuracy and generation efficiency of our model. Finally, Section 6 provides a summary and discusses future research directions.

II. DATA SIMULATION

This study constructs a dataset of simulated BNS gravitational waveforms to train a cAE. The dataset spans a broad range of physical parameters (Θ), including component masses, spins, and tidal deformability, and provides the corresponding amplitude and phase representations. This formulation enhances the efficiency of deep learning models in capturing waveform structures and their dependencies on Θ.

A. Waveform Representation

Gravitational waves are typically characterized by two polarization components, h_+ and $h_\times$, expressed as

$$h(t) = h_+(t) + ih_\times(t). \tag{1}$$

However, directly learning $h_+(t)$ and $h_\times(t)$ in the time domain is computationally demanding and may hinder training convergence due to waveform complexity. To improve learning efficiency, we adopt an amplitude-phase representation, where h_+ is treated as the real part and $h_\times$ as the imaginary part. The corresponding amplitude $A(t)$ and cumulative phase $\Phi(t)$ are given by

$$A(t) = \sqrt{h_+^2 + h_\times^2}, \quad \Phi(t) = \tan^{-1}\left(\frac{h_\times}{h_+}\right). \tag{2}$$

This representation reduces data dimensionality while enhancing physical interpretability. The amplitude $A(t)$ captures the overall intensity variation of the gravitational wave, while the cumulative phase $\Phi(t)$ describes its temporal evolution, offering a depiction of the underlying dynamics. To further standardize waveform properties, we apply phase normalization,

$$\Phi(t) = \Phi(t) - \Phi(t_0), \tag{3}$$

which aligns all waveforms to an initial phase of zero. This adjustment improves dataset consistency and stabilizes model training by minimizing phase discrepancies across waveforms, facilitating a more effective learning of parameter dependencies in waveform evolution.

B. System Parameter Selection

Previous studies on gravitational waveform modeling have largely focused on BBH systems, while investigations of BNS waveforms remain relatively limited. Moreover, most deep learning models assume either non-spinning neutron stars or perfectly aligned spins, without systematically accounting for precession effects. Tidal deformation, which significantly influences the phase evolution of BNS waveforms, is often simplified using point-mass approximations, leading to the omission of crucial tidal contributions. A further limitation lies in the restricted parameter space of existing datasets. For instance, the mass range is typically constrained to $[1.2, 2.0]M_\odot$, spin magnitudes remain small ($|S| < 0.5$), and the tidal deformability parameters Λ_1, Λ_2 have limited coverage, reducing the ability to capture variations across different EOS. These constraints hinder the generalization capability of deep learning models and limit their applicability in real GW detection. To address these challenges, we develop a machine learning framework that systematically incorporates both precession and tidal effects, enhancing waveform modeling for BNS systems.

To ensure the model effectively learns the key features of BNS waveforms, we select a set of Θ spanning a broad region of the parameter space, as summarized in TABLE I. Specifically, we set the luminosity distance to 1 Mpc, and fix both the inclination angle and the coalescence phase to 0.

Θ	**Range**
m_1	Uniform$[1,3]M_\odot$
m_2	Uniform$[1,3]M_\odot$
S_{1x}	Uniform$[-0.8, 0.8]$
S_{1y}	Uniform$[-0.8, 0.8]$
S_{1z}	Uniform$[-0.8, 0.8]$
S_{2x}	Uniform$[-0.8, 0.8]$
S_{2y}	Uniform$[-0.8, 0.8]$
S_{2z}	Uniform$[-0.8, 0.8]$
Λ_1	Uniform$[0, 500]$
Λ_2	Uniform$[0, 500]$

TABLE I: Range of Θ for the BNS system in the training dataset ($m_2 < m_1$).

C. Construction of Dataset

We construct a dataset of gravitational waveforms for BNS systems to train the cAE. The dataset comprises 3×10^5 samples generated using the IMRPhenomXP_NRTidalv2 waveform model, which incorporates both precession and tidal effects. The data generation process consists of parameter sampling, waveform computation, data preprocessing and normalization. Θ of the BNS system are drawn from uniform distributions, which is shown in TABLE I. The time-domain GW signals $h_+(t)$ and $h_\times(t)$ are computed using `pycbc.waveform.get_td_waveform`[39], followed by trimming to remove leading and trailing zero values. The amplitude $A(t)$ and phase $\Phi(t)$ are then computed using Eq. (2), as shown in FIG. 1. To maintain data uniformity, waveforms are standardized and zero-padded to a fixed duration of 2 seconds with a sampling rate of 4096 Hz, resulting in 8192 points per sample. Each waveform segment is extracted from the final 2 seconds before the ringdown phase, ensuring that the dataset captures the complete merger and ringdown stages while also covering part of the inspiral phase. The 2-second simulated waveform is sufficiently long to encompass the stage of prominent tidal effects preceding the merger [40], enabling the model to learn the characteristic evolution of waveforms across different dynamical regimes.

The dataset consists of three components: X_{train}, which contains the BNS system's Θ as input features; y_A, representing the amplitude data; and y_Φ, representing the phase data. During cAE training, we normalize the data to ensure stability and consistency. The X_{train} are processed using Min-Max Normalization [41], which rescales the data to the range $[0, 1]$, ensuring a uniform scale across different parameters and improving training stability:

$$X' = \frac{X - X_{\min}}{X_{\max} - X_{\min}}, \tag{4}$$

where X represents the original data, $X_{\min}$ and $X_{\max}$ are the minimum and maximum values of each parameter, and X' is the normalized data. For y_A and y_Φ, we apply standardization [42], which ensures zero mean and unit variance to eliminate scale differences and enhance training stability:

$$X' = \frac{X - \mu}{\sigma}, \tag{5}$$

where μ and σ denote the mean and standard deviation of the data, respectively. Since the amplitude and phase exhibit distinct evolution patterns, two separate cAEs are trained: one for learning a compact representation and reconstruction of y_A, and another for modeling y_Φ. During training, X_{train} is provided as a conditional variable to the autoencoder, ensuring that the latent representation z effectively captures the dependence of waveforms on Θ.

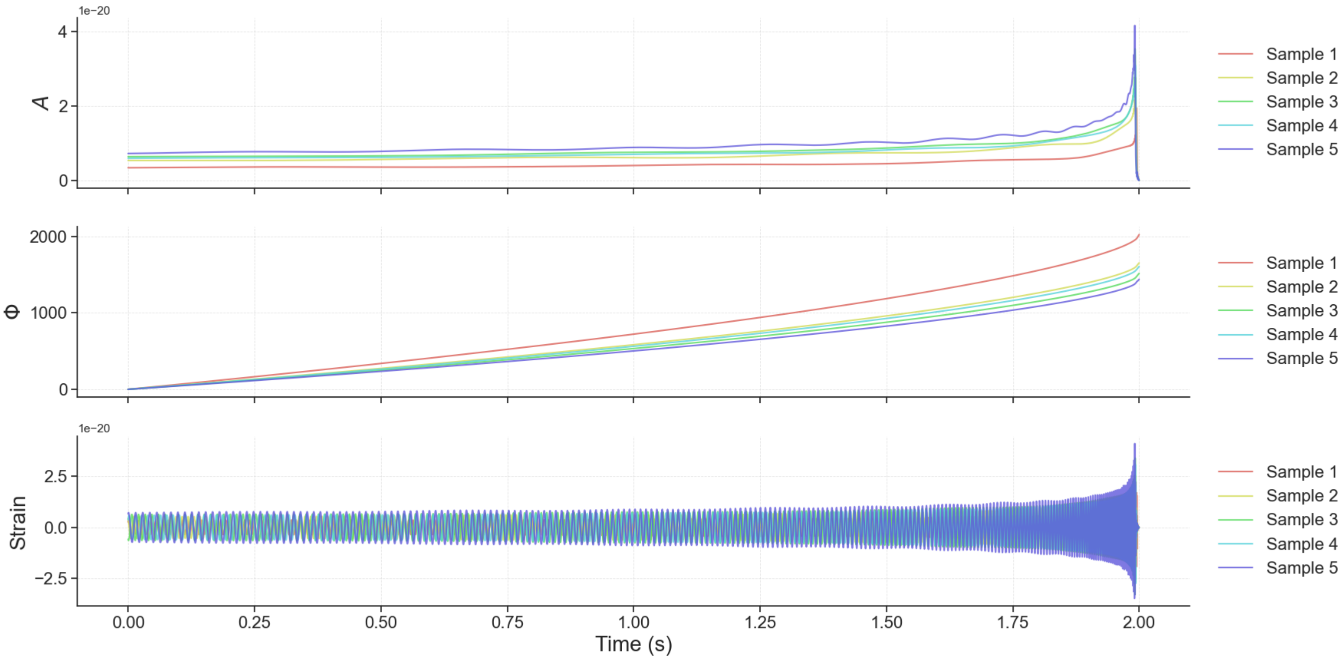

FIG. 1: Input samples in time domain. Top: amplitude curve $A(t)$; middle: phase curve $\Phi(t)$; bottom: waveform strain $h(t)$.

III. AUTOENCODER AND CONDITIONAL AUTOENCODER

The autoencoder (AE) is an unsupervised learning model widely used for data dimensionality reduction, feature extraction, and generative tasks. It consists of an encoder and a decoder, learning a low-dimensional representation of the data by minimizing reconstruction error. The variational autoencoder (VAE) extends this framework by introducing probabilistic modeling, enforcing a smoother latent variable distribution, which enhances the generative capability. The cAE further incorporates external conditional constraints, enabling the model to generate samples corresponding to specific data distributions based on input conditions, making it particularly relevant for GW waveform modeling.

This section first introduces the fundamental concepts of AE, VAE, and cAE, discussing their applicability to GW waveform generation. Subsequently, we provide a detailed description of the proposed cAE-based waveform generation framework, including the separate cAE architectures designed for phase and amplitude modeling, along with their respective hyperparameter settings.

A. Concepts of Autoencoder and Conditional Autoencoder

We employ autoencoders (AEs) [43] to reduce the dimensionality of complex GW waveforms (Amplitude A and Phase Φ) while ensuring accurate reconstruction. As shown in FIG. 2a, an AE consists of an input $h^{(i)}$ (A or Φ), an encoder $q_\alpha(z \mid h)$, a latent variable $z^{(i)} \in \mathbf{R}^d$, and a decoder $p_\beta(\hat{h} \mid z)$. The encoder projects the input (A or Φ) into a lower-dimensional latent space $z^{(i)}$, where the dimension d of $z^{(i)}$ can be adjusted based on specific task requirements. The decoder then reconstructs the $\hat{h}^{(i)}$ from the latent representation through an upsampling process. The α and β refers to the learned model parameters, such as weights and biases, obtained after training. To measure the similarity between the reconstructed $\hat{h}^{(i)}$ and the target $h^{(i)}$, the AE employs the mean squared error (MSE) as the reconstruction loss:

$$L_{\mathrm{MSE}} = \frac{1}{N}\sum_{i=1}^{N}\left\|h^{(i)} - \hat{h}^{(i)}\right\|^2, \tag{6}$$

where N is the total number of training samples, $h^{(i)}$ represents the target (A or Φ), and $\hat{h}^{(i)}$ is the reconstructed A or Φ. By minimizing L_{MSE}, the model updates its weights and biases, ensuring that $\hat{h}^{(i)}$ closely approximates $h^{(i)}$. Unlike traditional linear methods such as PCA [44], autoencoders (AEs) can capture the nonlinear features of GW signals more effectively [45]. While PCA is efficient for simple signals, its linear projections may miss important features in the nonlinear phases of GW evolution [46, 47]. In contrast, AEs reduce dimensionality through nonlinear mappings, preserving key physical features such as orbital dynamics, tidal effects, and ringdown. This enables better generalization, parameter recovery, and interpolation across the waveform space [48, 49]. FIG. 2b illustrates the structure of a VAE [50].

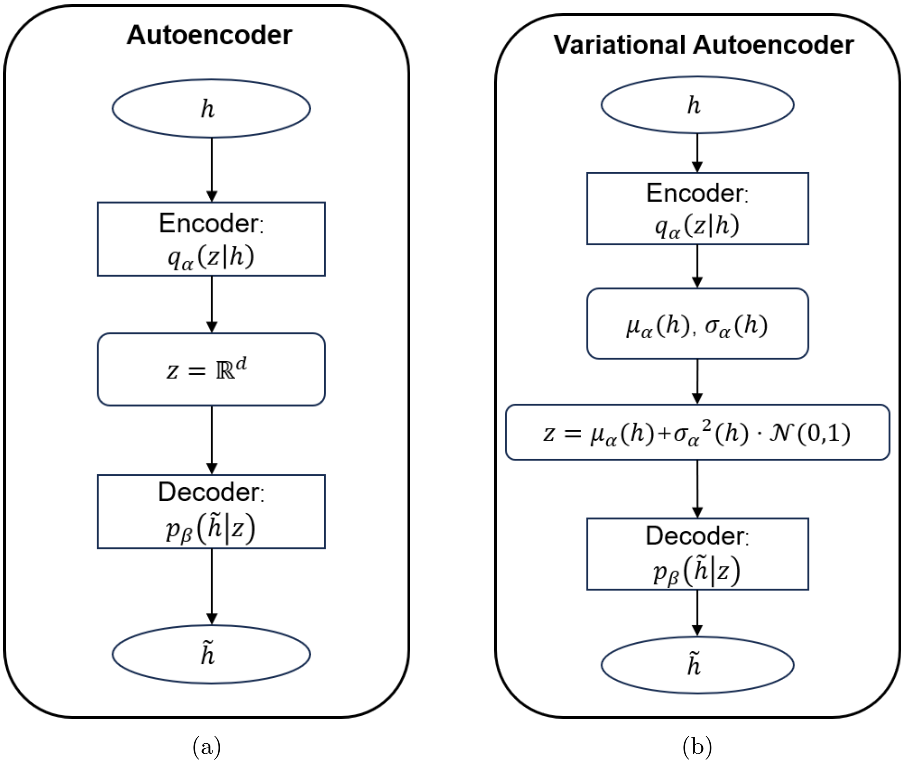
Autoencoder
h
Encoder: $q_\alpha(z|h)$
$z = \mathbb{R}^d$
Decoder: $p_\beta(\tilde{h}|z)$
$\tilde{h}$
(a)
Variational Autoencoder
h
Encoder: $q_\alpha(z|h)$
$\mu_\alpha(h)$, $\sigma_\alpha(h)$
$z = \mu_\alpha(h)+{\sigma_\alpha}^2(h) \cdot \mathcal{N}(0,1)$
Decoder: $p_\beta(\tilde{h}|z)$
$\tilde{h}$
(b)

FIG. 2: (a) Structure of an AE. (b) Structure of a variational VAE.

Unlike standard AEs, VAEs introduce probabilistic modeling between the encoder and decoder, ensuring that the latent variable $z^{(i)}$ is not a fixed deterministic value but is instead sampled from a distribution defined by the encoder's output mean $\mu_\alpha(h^{(i)})$ and variance $\sigma^2_\alpha(h^{(i)})$. Specifically, VAEs utilize the reparameterization trick to obtain latent variables:

$$z^{(i)} = \mu_\alpha(h^{(i)}) + \sigma_\alpha(h^{(i)}) \cdot \epsilon, \quad \epsilon \sim \mathcal{N}(0, I). \tag{7}$$

This approach allows gradients to propagate through the sampling process, making it possible to optimize the network using gradient-based methods. The VAE training objective consists of the reconstruction loss and the Kullback-Leibler (KL) divergence loss [51, 52]. The reconstruction loss measures the difference between the decoder's output $\hat{h}^{(i)}$ and the input waveform $h^{(i)}$, typically computed using the negative log-likelihood:

$$L_{\text{recon}} = \mathbb{E}_{q_\alpha(z|h)} \left[-\log p_\beta(\hat{h} \mid z) \right]. \tag{8}$$

The KL divergence loss ensures that the learned latent variable distribution $q_\alpha(z \mid h)$ approximates a predefined prior distribution, typically a standard normal distribution $p(z) = \mathcal{N}(0, I)$:

$$L_{\text{KL}} = D_{\text{KL}} \left(q_\alpha(z \mid h) \| p(z) \right). \tag{9}$$

The final VAE objective function is given by:

$$L_{\text{VAE}} = L_{\text{recon}} + \kappa L_{\text{KL}}, \tag{10}$$

where the hyperparameter κ controls the weight of the KL divergence loss, regulating the structure of the latent space.

Although traditional AEs and VAEs perform well in capturing the low-dimensional structure and nonlinear features of data, their generative processes typically rely solely on the data itself. As a result, they lack the capacity to explicitly incorporate known physical priors into the latent representations. In other words, standard AE/VAE models in unsupervised learning tend to capture the dominant variations in the data, but they cannot guarantee that the generated waveforms strictly adhere to physical constraints. To address this limitation and further enhance the physical interpretability and controllability of waveform generation, we introduce the cAE [53]. In the cAE framework, additional physical parameters Θ (as shown in TABEL I) are incorporated as conditional inputs and jointly mapped with waveform data into a low-dimensional latent space. In this manner, the cAE not only inherits the advantages of AE/VAE in nonlinear dimensionality reduction and data reconstruction, but also enables the explicit embedding of physical constraints into the latent variables, thereby generating waveforms that better reflect realistic astrophysical properties.

Our cAE employs a dual-encoder structure: one encoder processes the original h, while the other encodes the Θ, generating latent representations $z_{A/\Phi}$ and z_Θ, respectively. These are then mapped in the decoder to reconstruct the waveform $\hat{h}$. The total loss of training cAE consists of a reconstruction loss and a latent consistency loss:

$$L_{\mathrm{cAE}} = \frac{1}{N}\sum_{i=1}^{N}\left\|h_i - \hat{h}_i\right\|_{\mathrm{MAE}} + \lambda\frac{1}{N}\sum_{i=1}^{N}\left\|z_{A/\Phi,i} - z_{\Theta,i}\right\|^2_{\mathrm{MSE}}. \tag{11}$$

The first term measures the difference between the reconstructed waveform $\hat{h}_i$ and the target waveform h_i using Mean Absolute Error (MAE), while the second term ensures consistency between the latent representations $z_{A/\Phi,i}$ and $z_{\Theta,i}$ using Mean Squared Error (MSE). The hyperparameter λ balances the two losses, in our study, we fixed it as 1. In the following, we provide a detailed description of our model architecture.

B. Architecture and Hyperparameters of the Model

Our study employs the cAEs to model the amplitude and phase of GW waveforms from BNS mergers. The model consists of two independent cAE, each responsible for learning a low-dimensional representation of either the amplitude y_A or phase y_Φ and reconstructing waveforms conditioned on Θ. Each cAE comprises two encoders (Encoder 1 and Encoder 2) and a decoder. Encoder 1 processes the amplitude or phase data, while Encoder 2 encodes the Θ, and the two latent representations are combined in the latent space before being mapped back to a complete waveform by the decoder. The overall model architecture is shown in FIG. 3, where Training and Test sections correspond to the training and inference workflows, while the remaining sections detail the structural components.

As shown in FIG. 3, our framework consists of two main branches: one for waveform encoding and reconstruction, and one for encoding Θ. The goal is to align latent representations from both branches while ensuring accurate waveform reconstruction.

Encoder 1 is used independently for amplitude and phase inputs. Each encoder processes a normalized 1D data through a Conv1D layer with stride 2, followed by three ResNet blocks for local feature extraction and two Transformer blocks for capturing long-range dependencies. A global average pooling layer compresses the temporal dimension, and a final dense layer maps the features into a latent space (z_A or z_Φ).

Encoder 2 takes Θ (TABLE I) as input. These are passed through four fully connected layers, followed by two Transformer blocks. The output is projected into the same latent space as Encoder 1, producing z_Θ.

Decoder takes the latent variable from Encoder 1 and reconstructs the waveform. It expands the latent dimension via a dense layer, then applies two Transformer blocks and three upsampling ResNet blocks using transposed Conv1D layers, recovering the waveform shape.

Latent variables and loss functions: During training, both the waveform and the Θ are encoded into their respective latent representations, denoted as $z_{A/\Phi}$ and z_Θ. To ensure that the decoder can accurately reconstruct the input waveform and that both latent spaces are aligned, we define two loss components: First, the *reconstruction loss* is computed as the MAE between the input waveform x and the reconstructed waveform $\hat{h}$:

$$L_{\mathrm{rec}} = \frac{1}{N}\sum_{i=1}^{N}\left\|h^{(i)} - \hat{h}^{(i)}\right\|_{\mathrm{MAE}}. \tag{12}$$

Second, the *latent consistency loss* penalizes the difference between the latent vector produced by Encoder 1 (A/Φ) and Encoder 2 (Θ):

$$L_{\mathrm{latent}} = \frac{1}{N}\sum_{i=1}^{N}\left\|z^{(i)}_{A/\Phi} - z^{(i)}_{\Theta}\right\|^2_{\mathrm{MSE}}. \tag{13}$$

The total loss is then defined as a weighted sum of the two as Eq. (11):

$$L_{\mathrm{total}} = L_{\mathrm{rec}} + \lambda L_{\mathrm{latent}}, \tag{14}$$

where λ is a balancing coefficient. In our study, we set $\lambda = 1$ to equally weight reconstruction accuracy and latent alignment.

With the model architecture defined, we describe the training procedure and validation setup used to evaluate the model's performance in the following section.

IV. TRAINING AND VERIFICATION

Our model is trained using the Adam optimizer with an initial learning rate of 10^{-4}. To enhance training stability and convergence speed, the following learning rate scheduling mechanism is implemented: if the validation loss (val_loss) does not improve for 7 consecutive epochs, the learning rate is reduced by a factor of 0.7, with a minimum threshold of 10^{-8}. Additionally, an early stopping strategy is employed to prevent overfitting—if the validation loss shows no significant improvement within 15 epochs, training is automatically halted, and the model parameters are reverted to those corresponding to the best validation performance. The training is conducted on a single NVIDIA RTX 3090 GPU, with Amplitude (A) and phase (Φ) models trained separately. The total training process took approximately one week on a single RTX 3090. The dataset consists of 3×10^5 samples, with 90% used for training and 10% for validation. The batch size is set to 10, and the maximum training epochs are limited to 500. The training of both the amplitude and phase models took approximately a total of seven days. FIG. 4 illustrates the training loss evolution for both the amplitude and phase models.

To evaluate the accuracy of cAE-generated waveforms, we compute the mismatch between the model-generated

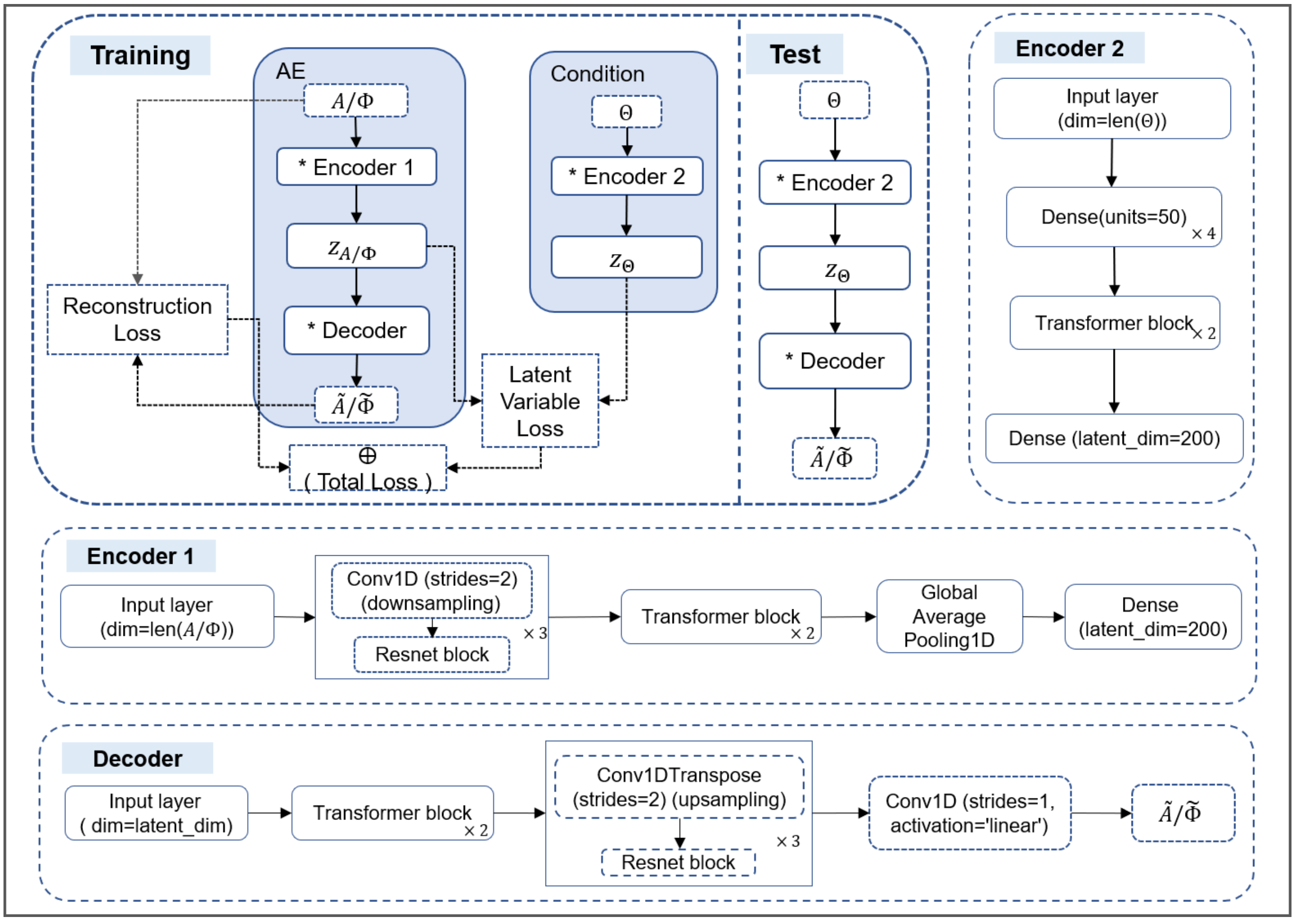

FIG. 3: Training and testing framework of the our model, along with detailed structures of individual components, the structure of the Transformer and ResNet block are shown in Appendix A (FIG 10).

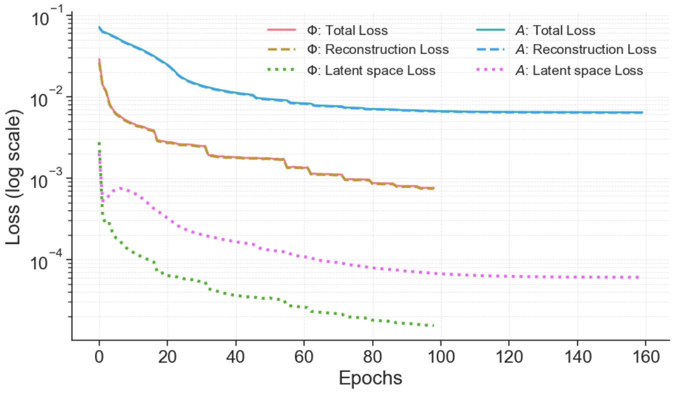

FIG. 4: Training and validation loss curves for the amplitude and phase models.

waveforms and the IMRPhenomXP_NRTidalv2 target waveforms. The evaluation is based on two key metrics: Overlap [54–56] and Mismatch, which quantify the waveform reconstruction quality. The analysis is conducted in the frequency domain after applying a Fourier transform to the time-domain waveforms, allowing for a more effective comparison of waveform similarities. In GW data analysis, the inner product of two waveforms is typically defined as a noise-weighted integral over the frequency domain, incorporating the power spectral density $S_n(f)$:

$$\langle h_1 \mid h_2 \rangle = 4\mathrm{Re} \int_{f_{\min}}^{f_{\max}} \frac{\tilde{h}_1(f)\,\tilde{h}_2(f)}{S_n(f)}\,df, \tag{15}$$

where $\tilde{h}_1(f)$ and $\tilde{h}_2(f)$ are the Fourier transforms of $h_1(t)$ and $h_2(t)$, respectively, and $S_n(f)$ represents the power spectral density (PSD) of the detector noise. This weighted inner product provides a measure of how well two waveforms match in the presence of detector noise. Since our task does not require a realistic noise model, we set $S_n(f) = 1$.

To eliminate the influence of normalization, each waveform is rescaled to satisfy the unit-norm condition:

$$\hat{h}(t) = \frac{h(t)}{\sqrt{\langle h \mid h \rangle}}. \tag{16}$$

The Overlap between two waveforms is then computed by maximizing the inner product over different time shifts

t_c and phase shifts ϕ_c:

$$O(h_1, h_2) = \max_{t_c, \phi_c} \frac{\langle \hat{h}_1 \mid \hat{h}_2 \rangle}{\sqrt{\langle \hat{h}_1 \mid \hat{h}_1 \rangle \langle \hat{h}_2 \mid \hat{h}_2 \rangle}}. \tag{17}$$

Based on this Overlap metric, the Mismatch is defined as:

$$M(h_1, h_2) = 1 - O(h_1, h_2). \tag{18}$$

Here, $M(h_1, h_2)$ quantifies the dissimilarity between the two waveforms, where lower values indicate a higher similarity between the model-generated waveforms and the target physical waveforms.

V. RESULTS AND ANALYSIS

In this section, we present the accuracy and efficiency of the model on the test set. Furthermore, we analyze various factors that influence the precision of the generated waveforms.

A. Mismatch Evaluation

To assess the accuracy of cAE-generated waveforms, we regenerated 3×10^5 test samples based on the Θ ranges listed in TABLE I and computed their mismatch values . FIG. 5 presents the mismatch distribution for h_+ and $h_\times$, showing that their averaged mismatch values are 3.9717×10^{-3} and 3.9770×10^{-3}, respectively, corresponding to an average waveform accuracy of 99.6%, considering both precession and tidal effects in BNS. Some more detailed charts illustrating the reconstruction results for samples with different orbital cycle numbers are provided in FIG. 11-FIG. 14 in the Appendix A.

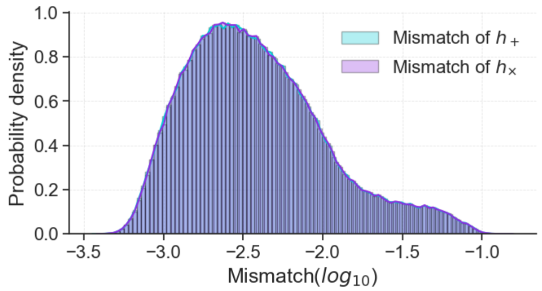

FIG. 5: The mismatch distribution of the test sample.

To further analyze the factors influencing mismatch, we computed the orbital cycle number for each sample. The time-domain signal $s(t)$ undergoes a Hilbert transform to obtain its analytic representation[57]:

$$s_a(t) = s(t) + i\,\mathcal{H}\{s(t)\}, \tag{19}$$

where $\mathcal{H}\{\cdot\}$ denotes the Hilbert transform. The instantaneous phase is then extracted from the analytic signal:

$$\phi(t) = \arg\big(s_a(t)\big). \tag{20}$$

To eliminate phase discontinuities, we apply phase unwrapping to obtain a monotonic phase function $\tilde{\phi}(t)$ and compute the total phase difference:

$$\Delta\phi = \tilde{\phi}(T) - \tilde{\phi}(0). \tag{21}$$

Finally, the orbital cycle number is given by:

$$\mathrm{NumCycles} = \frac{\Delta\phi}{2\pi}. \tag{22}$$

FIG. 6a shows the test set's cycle number distribution with a averaged cycle number of 265 and 68% of the samples falling within the range of 231 to 307 cycles. As shown in FIG. 6b, most samples cluster around 250 cycles, where the mismatch remains relatively low. However, when the cycle number exceeds 300, the mismatch begins to increase. This trend, consistent with FIG. 6b, indicates that an increasing cycle number significantly impacts the mismatch, particularly when exceeding 300, where the model's reconstruction accuracy deteriorates.

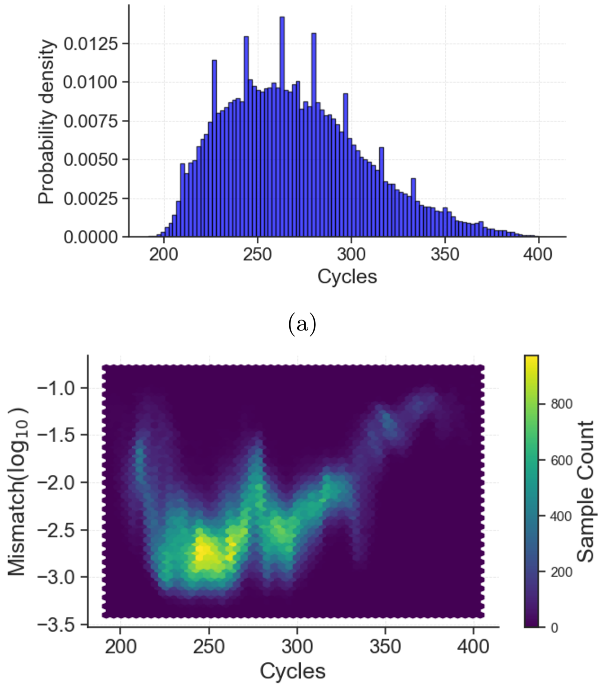

(a)

(b)

FIG. 6: (a) The test set's cycle number distribution. (b) Relationship between the number of cycles and mismatch ($\log_{10}$) in the test set. The color bar indicates the number of samples in each hexagonal bin.

As shown in FIG. 7a, lower-mass binaries exhibit more waveform cycles, whereas increasing mass results in fewer

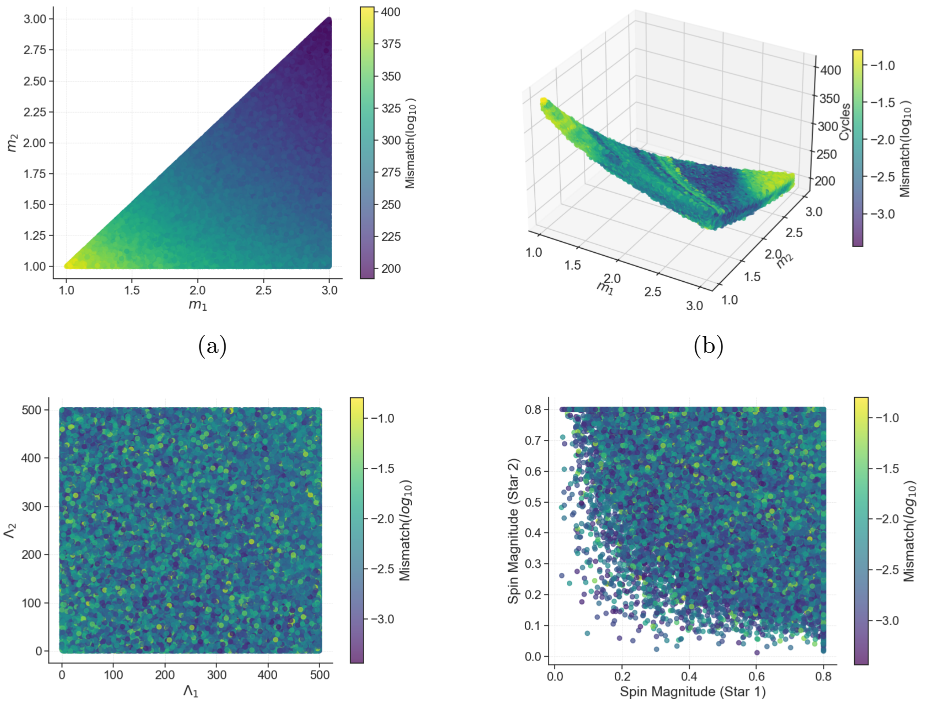

(a)

(b)

(c)

(d)

FIG. 7: (a) Relationship between binary mass and cycle number in the test set. (b) Relationship between binary mass, cycle number, and mismatch. (c) Relationship between tidal deformability and mismatch in the test set. (d) Relationship between spin parameters and mismatch.

cycles, so that mismatch values are relatively high in both low-mass (high-cycle) and high-mass (low-cycle) regions (as shown in FIG. 7b). This trend is primarily due to two factors: (1) as the number of waveform cycles increases, the time-domain complexity of the signal rises, making it more challenging for the network to learn; (2) high-cycle samples are underrepresented in the training set, reducing the model's generalization ability in this region. When the cycle number falls between 200 and 250, the mismatch is approximately 3.1×10^{-3}, increasing slightly to 3.2×10^{-3} in the 250–300 range. However, a significant rise to 7.2×10^{-3} is observed for 300–350 cycles, and once the cycle number exceeds 350, the mismatch escalates sharply, reaching 4.6×10^{-2} in the 350–400 range.

In order to investigate the impact of tidal deformation and spin parameters on mismatch, we plotted the mismatch distributions under different tidal deformability and total spin conditions in FIG. 7. FIG. 7c shows that the mismatch distribution under different tidal deformabilities is random, which suggests that, under the conditions of this study, tidal deformability has a negligible impact on waveform generation accuracy. Similarly, FIG. 7d indicates that spin parameters also exhibit a weak correlation with mismatch, implying that precession effects do not significantly degrade the model's waveform accuracy. This observation is further supported by FIG. 15 in the Appendix A, where no strong mismatch trend is observed in the joint distributions of spin and tidal deformability parameters.

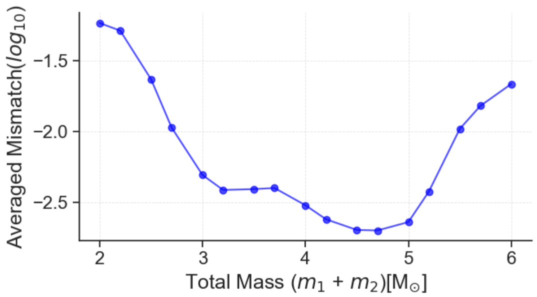

FIG. 8: Relationship between average mismatch and total mass in the test set.

Finally, we analyze the relationship between total mass and mismatch, as shown in FIG. 8. The results indicate that samples with total masses between $3.0 M_\odot$ and $5.0 M_\odot$ exhibit the lowest average mismatch. That is consistent with FIG. 7b, further confirming that our model achieves the highest accuracy when generating waveforms with total binary masses between $3.0 M_\odot$ and $5.0 M_\odot$ and cycles between 200 and 250. Additionally, the joint distribution of binary mass in FIG. 15 of the Appendix A reveals a clear trend of increasing mismatch in both high-mass and low-mass regions.

B. Waveform Generation Efficiency

To evaluate the efficiency of waveform generation, we compared the cAE model with several traditional waveform approximation methods by measuring the total computation time for different batch size. Specifically, we selected four widely used models: SpinTaylorT1, IMRPhenomPv2_NRTidal, IMRPhenomPv2_NRTidalv2, and IMRPhenomXP_NRTidalv2. All experiments were conducted using an NVIDIA RTX 3090 GPU and an Intel(R) Xeon(R) Silver 4214R CPU, with batch size ranging from 1 to 10,000. The results indicate that the cAE significantly outperforms traditional methods in computational efficiency, particularly for large-scale batch waveform generation.

For generating a single waveform, the cAE requires 0.12 s, which is shorter than SpinTaylorT1 (0.29 s), IMRPhenomPv2_NRTidalv2 [38] (0.39 s), IMRPhenomXP_NRTidalv2 (0.38 s), and IMRPhenomPv2_NRTidal [58] (0.62 s). For the large-scale generation of 10,000 waveforms, the cAE completes the task in only 7.48 s, while SpinTaylorT1, IMRPhenomXP_NRTidalv2, IMRPhenomPv2_NRTidalv2, and IMRPhenomPv2_NRTidal require 486.86, 454.51, 462.87, and 497.75 s, respectively. This indicates that our model can efficiently accelerate waveform generation when generating large batch size. A detailed comparison of computation times is presented in FIG. 9 and TABLE II. Further analysis of total computation time across varying batch size reveals that the cAE exhibits near-sublinear scaling behavior. As the batch size increases from 1 to 10, 100, 500, 1,000, and 10,000, the total generation time modestly rises from 0.12 s to 0.12, 0.20, 0.50, 0.86, and 7.48 s, respectively. This scaling highlights the excellent efficiency and scalability of the cAE model for batch processing.

In contrast, traditional waveform approximation methods exhibit significantly steeper increases in total computation time as batch size grow. Specifically, SpinTaylorT1 computation time rises from 0.29 s (batch size = 1) to 486.86 s (batch size = 10,000). IMRPhenomPv2_NRTidal grows from 0.62 s to 497.75 s, IMRPhenomPv2_NRTidalv2 from 0.39 s to 462.87 s, and IMRPhenomXP_NRTidalv2 from 0.38 s to 454.51 s. These results underscore that without multi-core parallel optimization, traditional methods become notably less efficient compared to the cAE for large-scale waveform generation.

This advantage makes our model particularly suitable for real-time waveform generation and large-scale parameter space sampling, providing a new and feasible approach for efficient GW data analysis.

VI. SUMMARY AND DISCUSSION

This study presents an efficient gravitational waveform generation method based on a cAE and applies it to amplitude-phase modeling of BNS systems. Compared to traditional waveform approximation methods such as IMRPhenomXP_NRTidalv2, cAE significantly improves computational efficiency while maintaining high reconstruction accuracy. On a large-scale test dataset, the averaged waveform mismatch is 3.97×10^{-3}, corresponding to an average accuracy exceeding 99.6%. Even with precession and tidal effects, cAE maintains high precision across different Θ ranges, particularly in the high-cycle orbital evolution phase. In terms of efficiency, the cAE model demonstrates a significant advantage over traditional waveform approximation methods. For a single waveform, cAE requires only 0.12 seconds, compared to 0.38 seconds for IMRPhenomXP_NRTidalv2 and 0.62 seconds for IMRPhenomPv2_NRTidal, yielding speedups of approximately 3 to 5 times. As the batch size increases, this advantage becomes more pronounced. For 1,000 waveforms, cAE completes the task in 0.86 seconds, while IMRPhenomXP_NRTidalv2 and IMRPhenomPv2_NRTidal require 46.12 and 53.47 seconds, respectively—corresponding to speedups of around 54 and 62 times. When generating 10,000 waveforms, cAE requires only 7.48 seconds, compared to 454.51 seconds for IMRPhenomXP_NRTidalv2 and 497.75 seconds for IMRPhenomPv2_NRTidal, achieving speedups of over 60 times. These results suggest that cAE scales more efficiently with batch size compared to traditional methods. These results suggest that our cAE model is more efficient than traditional waveform approximation methods for generating waveforms at large batch size.

Additionally, this study constructs a large-scale BNS waveform dataset covering an extended physical parameter space, including mass, spin, and tidal deformation, allowing the model to learn waveform characteristics under complex physical conditions. To improve time-series modeling, the cAE architecture integrates ResNet and Transformer mechanisms, enhancing its ability to represent long-duration waveforms and reducing reconstruction errors in high-cycle orbital phases. This design improves generalization and offers new insights for high-precision waveform modeling.

Despite the progress achieved in this study, several aspects require further optimization. The analysis indicates a slight increase in mismatch for both high- and low-mass binaries. In high-mass systems, the short merger time limits the network's ability to capture waveform details, while the relatively small number of training samples may constrain generalization. Data augmentation or adaptive sampling could mitigate these effects. For low-mass binaries, the higher number of orbital cycles presents additional challenges for accurate waveform fitting, suggesting room for improvement in modeling long-term evolution. The model's performance under different spin and tidal deformation parameters shows less

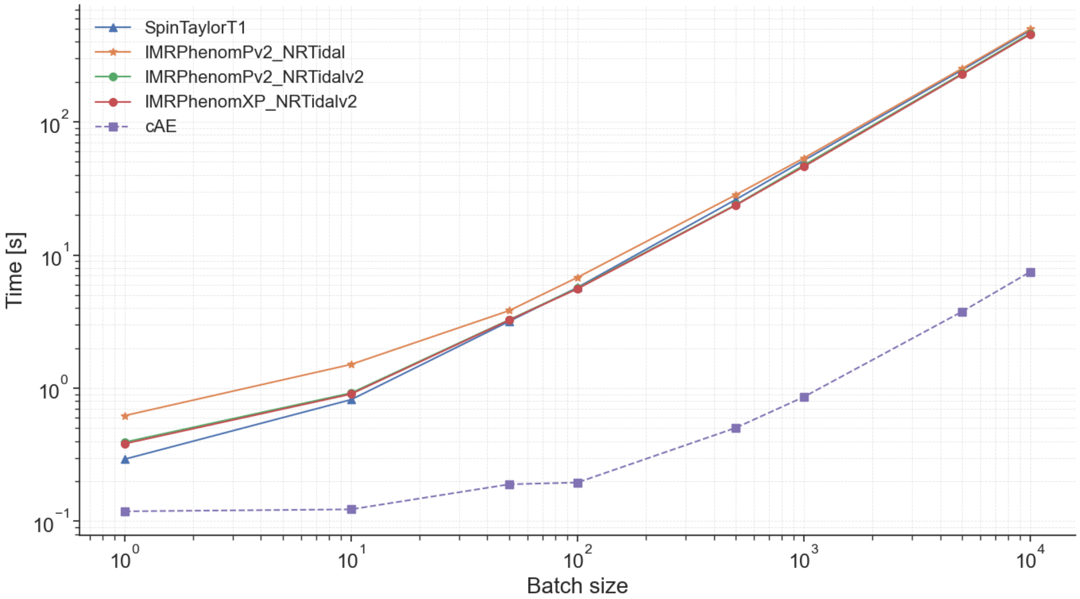

FIG. 9: Comparison of computation time between cAE and traditional waveform approximation. The horizontal axis represents the number of generated samples, while the vertical axis represents the computation time.

TABLE II: Waveform generation time (s) for different batch size using the cAE and some waveform approximation methods.

Batch size Approximants	1	10	50	100	500	1000	5000	10000
cAE	0.1188	0.1229	0.1895	0.1954	0.5030	0.8595	3.7589	7.4778
SpinTaylorT1	0.2926	0.8191	3.1774	5.7059	26.0688	51.3171	245.5291	486.8640
IMRPhenomPv2_NRTidal	0.6213	1.5070	3.8230	6.7868	28.2600	53.4714	251.7113	497.7530
IMRPhenomPv2_NRTidalv2	0.3925	0.9189	3.2646	5.6403	23.8314	47.2493	230.3046	462.8673
IMRPhenomXP_NRTidalv2	0.3823	0.9026	3.2442	5.5723	23.6224	46.1181	227.1048	454.5058

variation than expected, indicating that sensitivity to extreme parameter regions warrants further investigation. Future work will systematically analyze key factors influencing waveform generation to enhance physical consistency and generalization. While cAE significantly improves computational efficiency over traditional methods, further acceleration strategies, such as TensorRT[59, 60] or ONNX Runtime[61], could further reduce inference time, improving suitability for real-time GW analysis.

Several directions for future research emerge from this study. The impact of latent variable dimensionality on waveform accuracy and efficiency remains unexplored and will be systematically analyzed. Expanding the parameter space to include more complex sources, such as eccentric binaries and a broader range of spin and tidal effects, will further improve applicability. On the architectural side, advanced deep learning methods, including diffusion models [62] and Transformer variants [63], could enhance waveform generation accuracy and efficiency. Moreover, integrating deep learning with JAX-based acceleration techniques [64] may further improve computational efficiency. Additionally, Bayesian inference with neural networks for waveform generation could accelerate parameter estimation [65] for GW events.

In conclusion, the cAE-based waveform generation method proposed in this study offers an efficient and accurate approach to BNS waveform modeling. It shows strong potential for real-time data analysis, large-scale parameter estimation, and GW event identification. As deep learning continues to advance, data-driven methods are expected to play a growing role in GW astronomy, providing more precise and computationally efficient tools for signal modeling and fundamental physics research.

ACKNOWLEDGEMENTS

This work was supported by the National Key Research and Development Program of China (Grant No. 2021YFC2203004), the National Natural Science Foundation of China (Grant No. 12347101), and the Natural Science Foundation of Chongqing (Grant No. CSTB2023NSCQ-MSX0103).

[1] B. P. Abbott, R. Abbott, T. D. Abbott, M. R. Abernathy, F. Acernese, K. Ackley, C. Adams, T. Adams, P. Addesso, R. X. Adhikari, *et al.*, Observation of gravitational waves from a binary black hole merger, Physical review letters **116**, 061102 (2016).

[2] B. P. Abbott, R. Abbott, T. Abbott, F. Acernese, K. Ackley, C. Adams, T. Adams, P. Addesso, R. X. Adhikari, V. B. Adya, *et al.*, Gw170817: observation of gravitational waves from a binary neutron star inspiral, Physical review letters **119**, 161101 (2017).

[3] B. P. Abbott, R. Abbott, T. Abbott, S. Abraham, F. Acernese, K. Ackley, C. Adams, R. Adhikari, V. Adya, C. Affeldt, *et al.*, Gw190425: Observation of a compact binary coalescence with total mass $3.4\ m_{\odot}$, The Astrophysical Journal **892**, L3 (2020).

[4] R. Abbott, T. D. Abbott, S. Abraham, F. Acernese, K. Ackley, A. Adams, C. Adams, R. Adhikari, V. Adya, C. Affeldt, *et al.*, Observation of gravitational waves from two neutron star–black hole coalescences, The Astrophysical journal letters **915**, L5 (2021).

[5] D. Radice, A. Perego, K. Hotokezaka, S. A. Fromm, S. Bernuzzi, and L. F. Roberts, Binary neutron star mergers: mass ejection, electromagnetic counterparts, and nucleosynthesis, The Astrophysical Journal **869**, 130 (2018).

[6] L. Sagunski, J. Zhang, M. C. Johnson, L. Lehner, M. Sakellariadou, S. L. Liebling, C. Palenzuela, and D. Neilsen, Neutron star mergers as a probe of modifications of general relativity with finite-range scalar forces, Physical Review D **97**, 064016 (2018).

[7] E. E. Flanagan and T. Hinderer, Constraining neutron-star tidal love numbers with gravitational-wave detectors, Physical Review D—Particles, Fields, Gravitation, and Cosmology **77**, 021502 (2008).

[8] T. Hinderer, Tidal love numbers of neutron stars, The Astrophysical Journal **677**, 1216 (2008).

[9] J. Haislip, V. Kouprianov, D. Reichart, L. Tartaglia, D. Sand, S. Valenti, S. Yang, I. Arcavi, G. Hosseinzadeh, D. Howell, C. McCully, D. Poznanski, and S. Vasylyev, A gravitational-wave standard siren measurement of the hubble constant, Nature **551**, 85 (2017).

[10] K. Hotokezaka, P. Beniamini, and T. Piran, Neutron star mergers as sites of r-process nucleosynthesis and short gamma-ray bursts, International Journal of Modern Physics D **27**, 1842005 (2018).

[11] S. Bernuzzi, A. Nagar, M. Thierfelder, and B. Brügmann, Tidal effects in binary neutron star coalescence, Physical Review D—Particles, Fields, Gravitation, and Cosmology **86**, 044030 (2012).

[12] M. Hannam, P. Schmidt, A. Bohé, L. Haegel, S. Husa, F. Ohme, G. Pratten, and M. Pürrer, Simple model of complete precessing black-hole-binary gravitational waveforms, Physical review letters **113**, 151101 (2014).

[13] A. Bohé, L. Shao, A. Taracchini, A. Buonanno, S. Babak, I. W. Harry, I. Hinder, S. Ossokine, M. Pürrer, V. Raymond, *et al.*, Improved effective-one-body model of spinning, nonprecessing binary black holes for the era of gravitational-wave astrophysics with advanced detectors, Physical Review D **95**, 044028 (2017).

[14] J. Centrella, J. G. Baker, B. J. Kelly, and J. R. Van Meter, Black-hole binaries, gravitational waves, and numerical relativity, Reviews of Modern Physics **82**, 3069 (2010).

[15] T. W. Baumgarte and S. L. Shapiro, Numerical relativity and compact binaries, Physics Reports **376**, 41 (2003).

[16] F. Löffler, J. Faber, E. Bentivegna, T. Bode, P. Diener, R. Haas, I. Hinder, B. C. Mundim, C. D. Ott, E. Schnetter, *et al.*, The einstein toolkit: a community computational infrastructure for relativistic astrophysics, Classical and Quantum Gravity **29**, 115001 (2012).

[17] L. Blanchet, Gravitational radiation from post-newtonian sources and inspiralling compact binaries, Living reviews in relativity **17**, 2 (2014).

[18] A. Einstein, L. Infeld, and B. Hoffmann, The gravitational equations and the problem of motion, Annals of mathematics **39**, 65 (1938).

[19] A. Buonanno and T. Damour, Effective one-body approach to general relativistic two-body dynamics, Physical Review D **59**, 084006 (1999).

[20] T. Damour, A. Nagar, E. N. Dorband, D. Pollney, and L. Rezzolla, Faithful effective-one-body waveforms of equal-mass coalescing black-hole binaries, Physical Review D—Particles, Fields, Gravitation, and Cosmology **77**, 084017 (2008).

[21] A. Buonanno and T. Damour, Transition from inspiral to plunge in binary black hole coalescences, Physical Review D **62**, 064015 (2000).

[22] S. Khan, K. Chatziioannou, M. Hannam, and F. Ohme, Phenomenological model for the gravitational-wave signal from precessing binary black holes with two-spin effects, Physical Review D **100**, 024059 (2019).

[23] P. Ajith, S. Babak, Y. Chen, M. Hewitson, B. Krishnan, J. Whelan, B. Bruegmann, P. Diener, J. Gonzalez, M. Hannam, *et al.*, A phenomenological template family for black-hole coalescence waveforms, Classical and Quantum Gravity **24**, S689 (2007).

[24] S. Khan, S. Husa, M. Hannam, F. Ohme, M. Pürrer, X. J. Forteza, and A. Bohé, Frequency-domain gravitational waves from nonprecessing black-hole binaries. ii. a phenomenological model for the advanced detector era, Physical Review D **93**, 044007 (2016).

[25] Z. Doctor, B. Farr, D. Holz, and M. Purrer, Statistical gravitational waveform models: What to simulate next?, Physical Review D **96**, 10.1103/PhysRevD.96.123011 (2017).

[26] S. E. Field, C. Galley, J. Hesthaven, J. Kaye, and M. Tiglio, Fast prediction and evaluation of gravitational waveforms using surrogate models, ArXiv **abs/1308.3565**, 10.1103/PhysRevX.4.031006 (2013).

[27] A. Nagar and P. Rettegno, Efficient effective one body time-domain gravitational waveforms, Physical Review D 10.1103/PhysRevD.99.021501 (2018).

[28] T. e. a. Grimbergen, Generating higher order modes from binary black hole mergers with machine learning, arXiv preprint arXiv:2402.06587 (2024).

[29] O. G. e. a. Freitas, Nrsurnn3dq4: A deep learning powered numerical relativity surrogate for binary black hole waveforms, arXiv preprint arXiv:2412.06946 (2024).

[30] C.-H. Liao and F.-L. Lin, Deep generative models of gravitational waveforms via conditional autoencoder, arXiv preprint arXiv:2101.06685 (2021).

[31] R. e. a. Shi, Rapid eccentric spin-aligned binary black hole waveform generation based on deep learning, arXiv preprint arXiv:2411.14893 (2024).

[32] S. He, H. Wang, H. Li, and J. Zhao, Principle of machine learning and its potential application in climate prediction, Journal of Autonomous Intelligence 10.32629/jai.v4i1.483 (2021).

[33] D. George and E. A. Huerta, Deep learning for real-time gravitational wave detection and parameter estimation: Results with advanced ligo data, Physics Letters B **778**, 64 (2018).

[34] S. e. a. Schmidt, Machine learning gravitational waves from binary black hole mergers, Phys. Rev. D **103**, 043020 (2021).

[35] M. Dax, S. R. Green, J. Gair, N. Gupte, M. Pürrer, V. Raymond, J. Wildberger, J. H. Macke, A. Buonanno, and B. Schölkopf, Real-time inference for binary neutron star mergers using machine learning, Nature **639**, 49 (2025).

[36] T. e. a. Whittaker, Using machine learning to parametrize postmerger signals from binary neutron stars, arXiv preprint arXiv:2201.06461 (2022).

[37] A. J. K. e. a. Chua, Rapid generation of fully relativistic extreme-mass-ratio-inspiral waveform templates for lisa data analysis, arXiv preprint arXiv:2008.06071 (2020).

[38] T. Dietrich, A. Samajdar, S. Khan, N. K. Johnson-McDaniel, R. Dudi, and W. Tichy, Improving the nrtidal model for binary neutron star systems, Physical Review D **100**, 044003 (2019).

[39] A. Nitz *et al.*, gwastro/pycbc: Release 2.2.0 of pycbc (2023).

[40] S. Pal and R. K. Nayak, Tidal reconstruction of neutron star mergers from their late inspiral, The Astrophysical Journal **980**, 76 (2025).

[41] L. Rahmad Ramadhan and Y. Anne Mudya, A comparative study of z-score and min-max normalization for rainfall classification in pekanbaru, Journal of Data Science **2024**, 1 (2024).

[42] N. Singh and P. Singh, Exploring the effect of normalization on medical data classification, in *2021 International Conference on Artificial Intelligence and Machine Vision (AIMV)* (IEEE, 2021) pp. 1–5.

[43] G. E. Hinton and R. Zemel, Autoencoders, minimum description length and helmholtz free energy, Advances in neural information processing systems **6** (1993).

[44] A. Maćkiewicz and W. Ratajczak, Principal components analysis (pca), Computers & Geosciences **19**, 303 (1993).

[45] D. Cacciarelli and M. Kulahci, Hidden dimensions of the data: Pca vs autoencoders, Quality Engineering **35**, 741 (2023).

[46] E. J. Bloomer, *A principal component analysis of gravitational-wave signals from extreme-mass-ratio sources*, Ph.D. thesis, University of Glasgow (2010).

[47] M. P. Libório, O. Da Silva Martinuci, A. M. C. Machado, T. M. Machado-Coelho, S. Laudares, and P. Bernardes, Principal component analysis applied to multidimensional social indicators longitudinal studies: limitations and possibilities, GeoJournal **87**, 1453 (2022).

[48] S. Ladjal, A. Newson, and C.-H. Pham, A pca-like autoencoder, arXiv preprint arXiv:1904.01277 (2019).

[49] P. Nousi, S.-C. Fragkouli, N. Passalis, P. Iosif, T. Apostolatos, G. Pappas, N. Stergioulas, and A. Tefas, Autoencoder-driven spiral representation learning for gravitational wave surrogate modelling, Neurocomputing **491**, 67 (2022).

[50] D. P. Kingma, M. Welling, *et al.*, An introduction to variational autoencoders, Foundations and Trends® in Machine Learning **12**, 307 (2019).

[51] A. Asperti and M. Trentin, Balancing reconstruction error and kullback-leibler divergence in variational autoencoders, Ieee Access **8**, 199440 (2020).

[52] V. Prokhorov, E. Shareghi, Y. Li, M. T. Pilehvar, and N. Collier, On the importance of the kullback-leibler divergence term in variational autoencoders for text generation, arXiv preprint arXiv:1909.13668 (2019).

[53] C. Zhang, R. Barbano, and B. Jin, Conditional variational autoencoder for learned image reconstruction, Computation **9**, 114 (2021).

[54] B. J. Owen, Search templates for gravitational waves from inspiraling binaries: Choice of template spacing, Physical Review D **53**, 6749 (1996).

[55] B. J. Owen and B. S. Sathyaprakash, Matched filtering of gravitational waves from inspiraling compact binaries: Computational cost and template placement, Physical Review D **60**, 022002 (1999).

[56] B. F. Schutz, Data processing, analysis, and storage for interferometric antennas, in *The detection of gravitational waves* (Cambridge University Press, 1991) pp. 406–451.

[57] J. XIAO, Z. CHANG, *et al.*, Signal processing of projectile moving in-bore based on phase unwrapping algorithm, Journal of Projectiles, Rockets, Missiles and Guidance **32**, 189 (2012).

[58] T. Dietrich, S. Bernuzzi, and W. Tichy, Closed-form tidal approximants for binary neutron star gravitational waveforms constructed from high-resolution numerical relativity simulations, Physical Review D **96**, 121501 (2017).

[59] P. Chaturvedi, A. Khan, M. Tian, E. Huerta, and H. Zheng, Inference-optimized ai and high performance computing for gravitational wave detection at scale, Frontiers in Artificial Intelligence **5**, 828672 (2022).

[60] Z. Lijun, L. Yu, B. Lu, L. Fei, and W. Yawei, Using tensorrt for deep learning and inference applications, Journal of Applied Optics **41**, 337 (2020).

[61] N. Alizadeh and F. Castor, Green ai: A preliminary empirical study on energy consumption in dl models across different runtime infrastructures, in *Proceedings of the IEEE/ACM 3rd International Conference on AI Engineering-Software Engineering for AI* (2024) pp. 134–139.

[62] S. Mo and Y. Tian, Scaling diffusion mamba with bidirectional ssms for efficient image and video generation, ArXiv **abs/2405.15881**, 10.48550/arXiv.2405.15881 (2024).

[63] Z. Fei, M. Fan, C. Yu, D. Li, Y. Zhang, and J. Huang, Dimba: Transformer-mamba diffusion models, arXiv preprint arXiv:2406.01159 (2024).

[64] T. D. Edwards, K. W. Wong, K. K. Lam, A. Coogan, D. Foreman-Mackey, M. Isi, and A. Zimmerman, Differentiable and hardware-accelerated waveforms for gravitational wave data analysis, Physical Review D **110**, 064028 (2024).

[65] K. W. K. Wong, M. Isi, and T. Edwards, Fast gravitational-wave parameter estimation without compromises, The Astrophysical Journal **958**, 10.3847/1538-4357/acf5cd (2023).

Appendix A

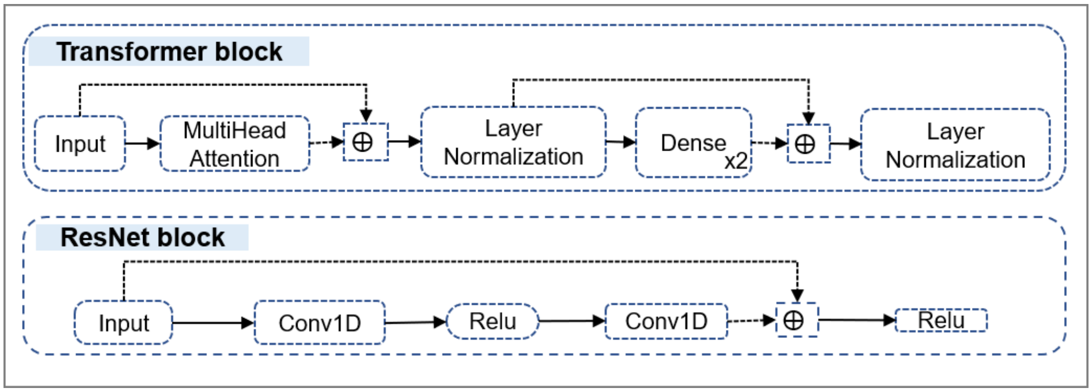

FIG. 10: Architectures of the Transformer and ResNet blocks used in our model.

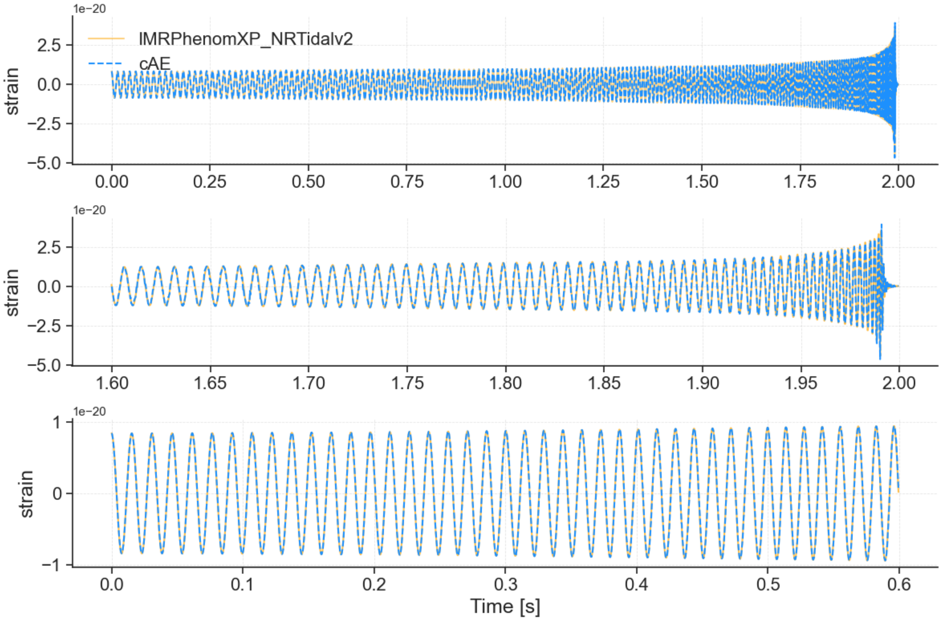

FIG. 11: Comparison of gravitational waveforms generated by the cAE (blue) and IMRPhenomXP_NRTidalv2 (yellow). The top subplot shows the full waveform over 0–2 s, with mismatch = 6.0×10^{-3} and 200 cycles. The middle subplot zooms into $t = 1.5998$–1.9995 s, with a local mismatch of 8.0×10^{-3}. The bottom subplot zooms into $t = 0$–0.5996 s, with a local mismatch of 5.95×10^{-4}. The test waveform parameters are $m_1 = 2.99M_\odot$, $m_2 = 2.84M_\odot$, $\Lambda_1 = 318.6$, $\Lambda_2 = 162.9$, $\mathrm{spin}_{1x} = -0.421$, $\mathrm{spin}_{1y} = -0.353$, $\mathrm{spin}_{1z} = -0.010$, $\mathrm{spin}_{2x} = 0.074$, $\mathrm{spin}_{2y} = -0.306$, $\mathrm{spin}_{2z} = -0.540$.

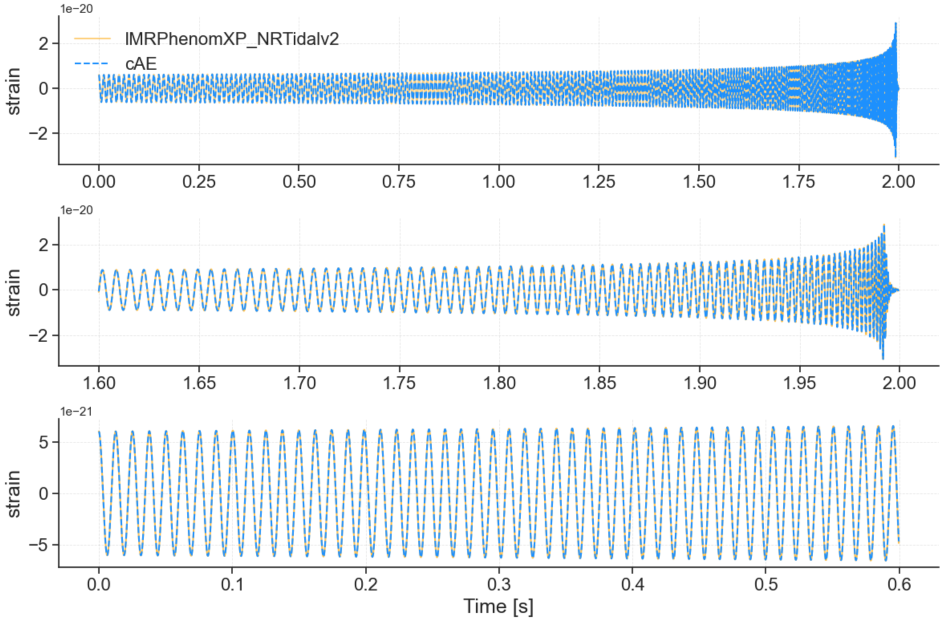

FIG. 12: The top subplot shows the full waveform over 0–2 s, with mismatch = 4.0×10^{-3} and 250 cycles. The middle subplot zooms into $t = 1.5998$–1.9995 s, with a local mismatch of 9.0×10^{-3}. The bottom subplot zooms into $t = 0$–0.5996 s, with a local mismatch of 1.54×10^{-4}. The test waveform parameters are $m_1 = 2.59M_\odot$, $m_2 = 1.83M_\odot$, $\Lambda_1 = 307.4$, $\Lambda_2 = 188.3$, $\text{spin}_{1x} = 0.145$, $\text{spin}_{1y} = -0.137$, $\text{spin}_{1z} = 0.164$, $\text{spin}_{2x} = -0.103$, $\text{spin}_{2y} = 0.295$, $\text{spin}_{2z} = 0.187$.

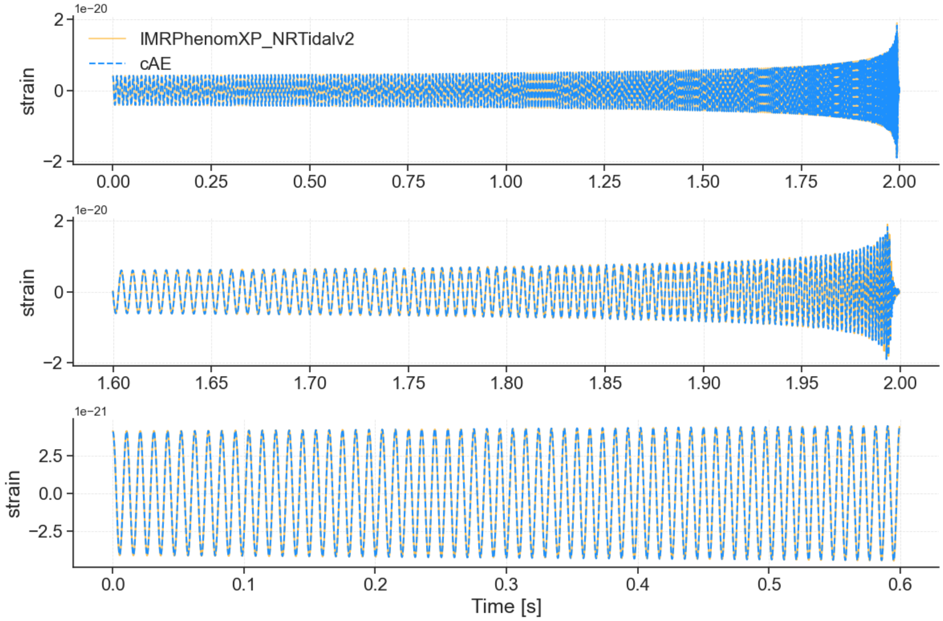

FIG. 13: The top subplot shows the full waveform over 0–2 s, with mismatch = 3.0×10^{-3} and 300 cycles. The middle subplot zooms into $t = 1.5998$–1.9995 s, with a local mismatch of 7.0×10^{-3}. The bottom subplot zooms into $t = 0$–0.5996 s, with a local mismatch of 4.03×10^{-4}. The test waveform parameters are $m_1 = 2.37M_\odot$, $m_2 = 1.11M_\odot$, $\Lambda_1 = 194.1$, $\Lambda_2 = 297.5$, $\text{spin}_{1x} = -0.067$, $\text{spin}_{1y} = 0.007$, $\text{spin}_{1z} = -0.516$, $\text{spin}_{2x} = 0.506$, $\text{spin}_{2y} = 0.392$, $\text{spin}_{2z} = -0.451$.

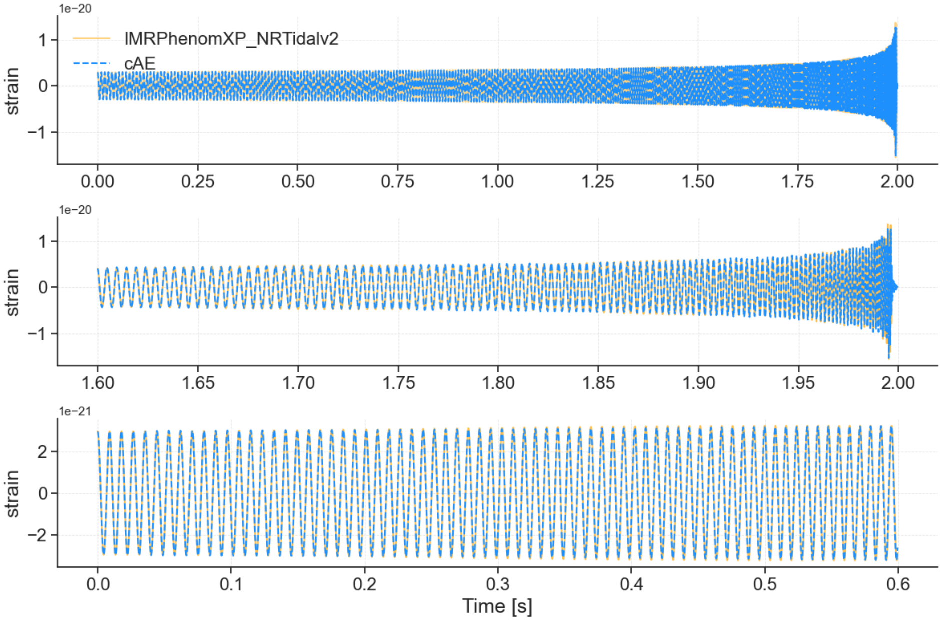

FIG. 14: The top subplot shows the full waveform over 0–2 s, with mismatch = 1.3×10^{-2} and 350 cycles. The middle subplot zooms into $t = 1.5998$–1.9995 s, with a local mismatch of 1.4×10^{-2}. The bottom subplot zooms into $t = 0$–0.5996 s, with a local mismatch of 4.0×10^{-3}. The test waveform parameters are $m_1 = 1.43 M_\odot$, $m_2 = 1.08 M_\odot$, $\Lambda_1 = 405.4$, $\Lambda_2 = 440.3$, $\text{spin}_{1x} = 0.608$, $\text{spin}_{1y} = 0.140$, $\text{spin}_{1z} = 0.501$, $\text{spin}_{2x} = 0.620$, $\text{spin}_{2y} = -0.221$, $\text{spin}_{2z} = -0.170$.

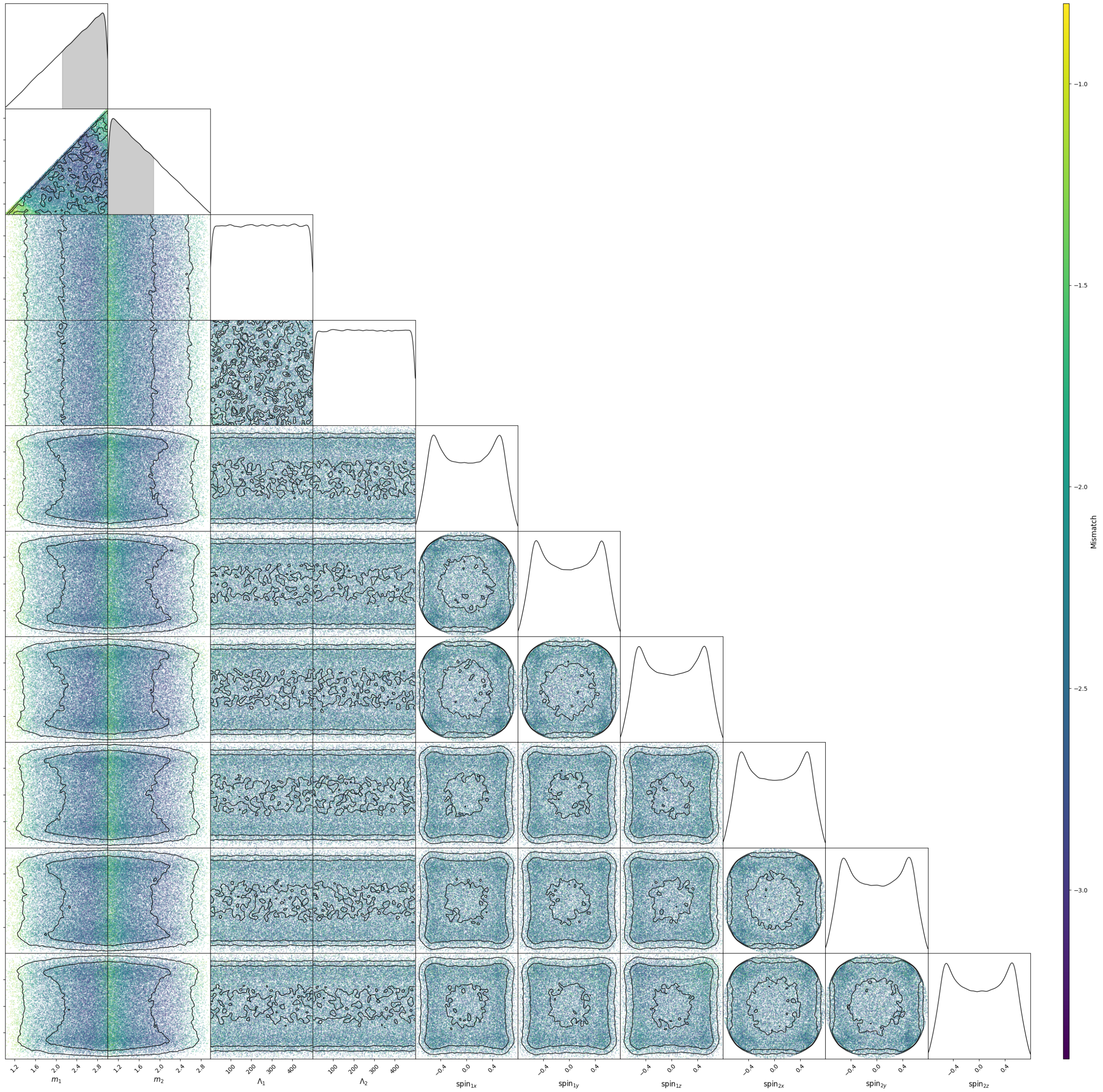

FIG. 15: Corner plot of 3×10^5 test set samples, showing the joint distribution of the 10-dimensional parameter space. The diagonal subplots display 1D histograms of each parameter, while the off-diagonal subplots show 2D joint distributions, where the color scale represents the corresponding mismatch value of each sample.